Draft version December 9, 2025
Typeset using LaTeX **twocolumn** style in AASTeX631

The quenched fraction of satellites around simulated Milky Way–mass galaxies

Francisco J. Mercado [1] Devontae C. Baxter [2] M. Katy Rodriguez Wimberly [3] Jorge Moreno [1,4] Coral Wheeler [5] Pratik Gandhi [6] Andrew Wetzel [7] Robert Feldmann [8] Lucas Tortora [9] and Jenna Samuel [10]

[1] *Department of Physics & Astronomy, Pomona College, Claremont, CA 91711, USA*
[2] *Department of Astronomy & Astrophysics, University of California, San Diego, 9500 Gilman Dr, La Jolla, CA 92093, USA*
[3] *Department of Physics % Astronomy, California State University, San Bernardino, San Bernardino, CA 92407, USA*
[4] *Carnegie Observatories, 813 Santa Barbara st, Pasadena, CA 91101, USA*
[5] *Department of Physics & Astronomy, California Polytechnic State University Pomona, Pomona, CA 91768, USA*
[6] *Department of Astronomy, Yale University, New Haven, CT 06520, USA*
[7] *Department of Physics & Astronomy, University of California, Davis, CA 95616, USA*
[8] *Department of Astrophysics, University of Zurich, Winterthurerstrasse 190, CH-8057 Zurich, Switzerland*
[9] *Institute of Astronomy and Kavli Institute for Cosmology, University of Cambridge, Madingley Road, Cambridge CB3 0HA, UK*
[10] *Department of Astronomy, The University of Texas at Austin3 Austin, TX 78712, USA*

ABSTRACT

We compare satellite quenched fractions across three cosmological simulation suites (FIREbox, the FIRE-2 zoom-ins, and IllustrisTNG50) and observational datasets from SAGA, ELVES, and the combined satellite population of the Milky Way and M31. To enable consistent comparisons, we select Milky Way–mass hosts with $M_{\rm halo} = 10^{11.9}$–$10^{12.2}\,M_\odot$ and satellites with stellar masses of 10^7–$10^{10}\,M_\odot$, applying uniform projected apertures and a common quenching definition. All three simulations reproduce the strong observed trend that lower-mass satellites are more likely to be quenched, closely matching the stellar-mass dependence seen in SAGA, ELVES, and the MW+M31 system. This agreement indicates that the mass dependence of satellite quenching is a robust outcome of contemporary galaxy-formation models. Radial trends, however, show meaningful differences. SAGA and ELVES exhibit gently declining quenched fractions with projected distance, reflecting strong environmental quenching at small radii. TNG50 most closely matches this behavior, FIREbox remains consistent with a nearly flat trend within uncertainties, and the FIRE-2 zoom-ins show suppressed inner quenched fractions driven almost entirely by their paired Milky Way–M31 hosts, which lack high-mass satellites and show strong radial segregation between star-forming and quenched systems. This environmental imprint suggests that host environment and assembly history can influence satellite quenching outcomes and may contribute to diversity across simulations. Overall, while the simulations consistently recover the stellar-mass dependence of quenching, their radial trends vary, highlighting the influence of host-halo conditions and motivating deeper exploration of how host environments shape satellite quenching.

Keywords: Dwarf Galaxies (416) – Scaling relations (2031) – Galaxy formation (595) – Galaxy evolution(594)

1. INTRODUCTION

Low-mass galaxies, with their shallow gravitational potentials, are highly susceptible to both *in situ* and *ex situ* processes that perturb the baryon cycle. This sensitivity makes them powerful probes of galaxy formation physics, including the galaxy–halo connection (Nadler et al. 2020; Mancera Piña et al. 2025), the epoch of reionization (Brown et al. 2014; Rodriguez Wimberly et al. 2019; McQuinn et al. 2024), and the co-evolution of galaxies and their environments (Weisz et al. 2011; Geha et al. 2012). A key empirical result from envi-

francisco.mercado@pomona.edu

ronmental studies is the strong dichotomy between low-mass galaxies ($M_\star < 10^9\ M_\odot$) that are isolated and those that are satellites of a more massive host. The former are almost exclusively star-forming (with only a few rare exceptions; Carleton et al. 2024; Li et al. 2024; Giovanelli et al. 2013; Jones et al. 2024; Mutlu-Pakdil et al. 2025; McQuinn et al. 2024), while the latter are far more likely to have ceased star formation (i.e., to be *quenched*).

Our understanding of how environment suppresses (or *quenches*) star formation in low-mass galaxies is derived primarily from observations of the Local Group. Studies of the MW and M31 satellite systems measure quenched fractions, inferred quenching timescales, and identified the dominant quenching mechanisms across nearly six decades in stellar mass (Wheeler et al. 2014; Wetzel et al. 2015; Rodriguez Wimberly et al. 2019; Fillingham et al. 2019). Extending these analyses beyond the Local Group require diverse observational strategies, including spectroscopic follow-up of faint satellites in nearby MW-like systems (Geha et al. 2017; Mao et al. 2021; Geha et al. 2024), volume-limited photometric surveys of nearby groups and Milky Way analogs (Carlsten et al. 2021, 2022; Greene et al. 2023; Meng et al. 2023), as well as machine-learning and statistical background-subtraction techniques applied to Sloan Digital Sky Survey data (Baxter et al. 2021).

Despite methodological differences, these studies paint a consistent picture: below $M_\star \sim 10^{9.5}\,M_\odot$, the satellite quenched fraction rises steadily toward lower stellar mass, reaching nearly 100% for systems below $M_\star \sim 10^5\,M_\odot$ where Ultra-Faint Dwarfs are predominantly quenched by reionization. Moreover, the Satellites Around Galactic Analogs (SAGA) and the Exploration of the Local VolumE (ELVES) surveys find that quenched fractions around MW-mass hosts remain low (∼0.2) at most host-centric radii within 300 kpc, with significant increases only in the innermost regions (Greene et al. 2023; Geha et al. 2024). These results provide a robust observational framework against which theoretical models can be tested.

A number of recent studies explore satellite quenching around MW-like hosts in cosmological simulations, consistently finding qualitative agreement with the observed mass-dependent trend (Simpson et al. 2018; Akins et al. 2021; Karunakaran et al. 2021; Font et al. 2022; Samuel et al. 2022; Engler et al. 2023; Christensen et al. 2024; Rodríguez-Cardoso et al. 2025). This agreement holds across diverse physics implementations, numerical resolutions, and choices of quenching diagnostics. For example, Samuel et al. (2022) examine quenching in the FIRE-2 MW-mass zoom-in simulations using time-resolved star formation histories and HI gas content, while other studies employ proxies such as youngest star-particle age or instantaneous specific star frmation rate (sSFR) (e.g., Simpson et al. 2018; Font et al. 2022; Engler et al. 2023). Time-averaged sSFR measurements tied to observational tracers (Hα, Ulra Violet and Far Ultra Violet) also yield similar qualitative trends (Akins et al. 2021; Karunakaran et al. 2021). Cross-code comparisons from the AGORA project show that this trend persists even when identical initial conditions are evolved with different hydrodynamic solvers (Rodríguez-Cardoso et al. 2025). Finally, Engler et al. (2023) use the Illustris TNG50 volume simulation (Nelson et al. 2018a; Pillepich et al. 2018a) to demonstrate that the same qualitative trend exists in a large cosmological sample, though the normalization of quenched fractions depends sensitively on how MW-like hosts are selected.

While the mass-dependent trend appears robust, considerably less attention has been devoted to whether simulations reproduce the observed radial dependence of quenching within $\sim 1\,r_{\rm vir}$. This is a key gap: environmental processes such as ram-pressure stripping, starvation, and tidal interactions are strongest near the host and should imprint clear signatures on radial quenched fraction profiles. Understanding the degree to which simulations capture this behavior is essential for disentangling the roles of internal physics and environment in satellite quenching.

Comparing satellite populations across simulations is inherently challenging: different halo-finding algorithms, feedback models, resolutions, and stellar-mass definitions mean that host halos selected to have the same mass are not strictly equivalent across suites. As a result, truly one-to-one comparisons require a level of homogenization beyond the scope of most existing studies. Here we instead take a first-order approach, showing that even under these mismatched but internally consistent definitions, the qualitative mass-dependent trend in quenched fractions remains robust.

In this paper, we examine satellite quenching as a function of both stellar mass and projected host-centric distance for Milky Way–mass galaxies across three simulation suites: FIREbox (Feldmann et al. 2023), the FIRE-2 MW-mass zoom-ins (Wetzel et al. 2016; Garrison-Kimmel et al. 2017, 2019a,b; Samuel et al. 2020), and IllustrisTNG50 (Nelson et al. 2018a; Pillepich et al. 2018a). We compare these predictions directly to satellite populations observed in the SAGA Survey (Geha et al. 2024), the ELVES Survey (Greene et al. 2023), and the combined Milky Way–M31 system (Wetzel et al. 2016). Despite substantial differences in resolution, cosmological volume, feedback implementations, and halo-finding architectures, all three simulations reproduce the observed mass dependence of satellite quenching. Their radial quenched fraction trends, however, show broader diversity, driven in particular by the paired FIRE-2 systems, indicating that satellite quenching is highly sensitive to the physical conditions of the host halo and to possible imprints of its larger-scale environment.

The remainder of this paper is organized as follows. Section 2 describes the simulations, observational datasets, host and satellite selection criteria, and methods for computing stellar and star formation properties. Section 3 presents satellite population statistics and quenched fraction trends across both simulations and observations. Section 4 interprets these results in the context of feedback physics, environmental processes, and host-galaxy properties. Section 5 summarizes our main findings and highlights future work, including two forthcoming studies that will quantify how host environment and host properties jointly regulate satellite quenching.

2. METHODOLOGY

2.1. *The FIRE-2 Galaxy Formation Model*

All FIRE simulations used in this work, including the cosmological volume FIREbox run and the FIRE-2 zoom-in suite, employ the FIRE-2 galaxy formation model (Hopkins et al. 2018). The simulations are run with the GIZMO code (Hopkins 2015) using the meshless finite-mass (MFM) hydrodynamics method. The FIRE-2 model includes explicit treatments of radiative cooling, star formation, and stellar feedback, and resolves the multiphase interstellar medium at sub-kiloparsec scales.

Gas cools radiatively to below 10^4 K and forms stars only in dense, self-gravitating, molecular, and self-shielding gas. FIREbox adopts a star-formation threshold of $n = 300\,\mathrm{cm}^{-3}$, and the zoom-in simulations use a threshold of $n = 1000\,\mathrm{cm}^{-3}$. Stellar feedback includes momentum, energy, mass, and metal return from Type Ia and core-collapse supernovae, winds from massive stars and asymptotic giant branch stars, radiation pressure, and both photo-electric and photo-ionization heating, following STARBURST99 stellar population models (Leitherer et al. 1999). Metal enrichment is tracked for 11 species, and the simulations assume a Kroupa IMF (Kroupa 2002). A spatially uniform and redshift-dependent UV and X-ray background (Faucher-Giguère et al. 2009) is applied.

Initial conditions for FIRE simulations are generated with MUSIC (Hahn & Abel 2011) using a flat ΛCDM cosmology consistent with Planck Collaboration et al. (2016). Although FIREbox and the zoom-in simulations differ in volume and resolution, they share identical baryonic physics. This allows direct comparisons across environments and host masses without introducing differences in subgrid prescriptions.

2.2. *The FIREbox Cosmological Volume Simulation*

FIREbox (Feldmann et al. 2023) is a periodic cosmological volume with a side length of 22.1 cMpc, evolved from $z = 120$ to $z = 0$ with 1024^3 gas and 1024^3 dark matter particles. The flagship `FB1024` run in this work has baryonic and dark matter particle masses of $m_\mathrm{b} = 6.3 \times 10^4\,M_\odot$ and $m_\mathrm{DM} = 3.3 \times 10^5\,M_\odot$, and adopts gas softening that is adaptive down to 1.5 pc. Star and dark matter particles have fixed softenings of 12 pc and 80 pc, respectively.

Although FIREbox is more modest in volume than some large cosmological simulations (e.g., Schaye et al. 2015; Pillepich et al. 2018a), it resolves scales from a few parsecs to several megaparsecs and includes environments ranging from voids to small galaxy groups with halo masses approaching $10^{13}\,M_\odot$. The simulation's high spatial resolution enatbles realistic modeling of interstellar physics, making it ideal for studying low-mass galaxy structure and environmental effects (Mercado et al. 2025; Klein et al. 2025; Benavides et al. 2025; Moreno et al. 2025).

2.2.1. *Halo identification in FIREbox*

We identify halos in FIREbox with the AMIGA Halo Finder (AHF; Knollmann & Knebe 2009), which reports virial quantities using a redshift-dependent overdensity threshold relative to the mean matter density (Bryan & Norman 1998). To place FIREbox on the same halo definition used for the FIRE-2 zoom-in simulations and TNG50, we convert these virial quantities to a spherical overdensity definition based on the mean matter density. We adopt the Bullock et al. (2001) mass–concentration relation and solve for the radius and enclosed mass corresponding to an average density of 200 times the mean matter density, yielding

$$r_\mathrm{halo} = r_\mathrm{200m}, \qquad M_\mathrm{halo} = M_\mathrm{200m}. \tag{1}$$

For satellite subhalos, AHF reports a truncation radius that encloses the gravitationally bound region. Because our analysis does not make use of satellite halo masses, we use only the AHF-provided positions and r_t values to identify bound satellites and compute their distances from host galaxies.

We adopt these halo radius and mass definitions for all simulation-based analyses throughout this work, ensuring consistency across FIREbox, the FIRE-2 zoom-in simulations, and TNG50.

2.3. *FIRE-2 Zoom-in Simulation Suite*

To complement the FIREbox volume, we analyze 13 high-resolution FIRE-2 zoom-in simulations of Milky Way or Andromeda mass galaxies at $z = 0$. These systems span a range of environments:

- Seven isolated systems from the Latte suite (Wetzel et al. 2016; Garrison-Kimmel et al. 2017; Samuel et al. 2020), with $M_{200\mathrm{m}} \sim 1$ to $2 \times 10^{12}\,M_\odot$ and no comparably massive neighbors within $5R_{200\mathrm{m}}$.
- Six paired systems from the ELVIS on FIRE suite (Garrison-Kimmel et al. 2017, 2019b), selected to reproduce Local Group like conditions with halo separations of 600 to 1000 kpc.

The isolated systems use dark matter particle masses of $3.5 \times 10^4\,M_\odot$ and initial gas or star particle masses of approximately $7 \times 10^3\,M_\odot$, with gas softening as small as 1 pc. The paired systems have roughly twice the mass resolution. Previous FIRE resolution studies show that such differences lead to only modest variations in galaxy properties and do not affect quenched fraction measurements in any significant way (Hopkins et al. 2018).

The FIRE-2 zoom-in simulations reproduce many observed features of the Local Group. These include stellar mass assembly histories, metallicity distributions, disk morphologies, and the structure of their satellite populations (Ma et al. 2017; Sanderson et al. 2020; Samuel et al. 2022; McCluskey et al. 2024). Their satellite stellar mass functions, radial distributions, and quenching timescales agree well with those observed for the Milky Way and M31 (Wetzel et al. 2016; Garrison-Kimmel et al. 2019a; Samuel et al. 2020). These comparisons provide confidence that the FIRE-2 MW mass systems serve as realistic analogs of Local Group environments.

2.3.1. *Halo identification in the FIRE-2 zooms*

Halos and subhalos in the FIRE-2 zoom-in simulations are identified using the ROCKSTAR halo finder (Behroozi et al. 2013), which performs adaptive refinement in phase space and uses temporal information to track halo evolution. ROCKSTAR directly reports spherical overdensity quantities relative to the mean matter density, which match the unified halo definition adopted for this work.

Because we apply a single halo-mass and halo-radius definition across all simulations, we do not recalculate or modify ROCKSTAR-reported quantities for the FIRE-2 zooms, nor do we attempt to re-derive FIREbox halos under ROCKSTAR conventions. This approach preserves the physically meaningful differences between halo finders while ensuring consistent host selection and distance measurements.

2.4. *IllustrisTNG: TNG50*

We also include Milky Way–mass hosts from the TNG50 simulation (Nelson et al. 2018b; Pillepich et al. 2018b; Springel et al. 2018), the highest-resolution run in the IllustrisTNG project. TNG50 evolves a $(51.7\,\mathrm{cMpc})^3$ cosmological volume with the moving-mesh AREPO code (Springel 2010), which solves ideal magnetohydrodynamics using a finite-volume Godunov scheme on a moving Voronoi mesh. The galaxy formation model includes metal-line cooling, star formation in a pressurized interstellar medium, kinetic and thermal energy injection from supernovae, and both thermal and kinetic modes of black hole feedback (Weinberger et al. 2017). The `TNG50-1` run used in this work reaches baryonic and dark matter mass resolutions of $8.5 \times 10^4\,M_\odot$ and $4.5 \times 10^5\,M_\odot$, with gravitational softening lengths of approximately 300 pc for collisionless particles.

We use TNG50 rather than the larger TNG100 or TNG300 volumes because its mass and spatial resolution are sufficient to robustly resolve the low-mass satellite population relevant for this study. In particular, TNG50 reaches baryonic and dark matter mass resolutions of $8.5 \times 10^4\,M_\odot$ and $4.5 \times 10^5\,M_\odot$, which allows us to model satellites down to the stellar masses probed by SAGA, ELVES, and the FIRE simulations. This makes TNG50 an appropriate comparison set for examining satellite quenching at the low-mass scales of interest.

2.4.1. *Halo identification in TNG50*

Halos in TNG50 are first identified using a Friends-of-Friends (FoF) algorithm (Davis et al. 1985), after which the SUBFIND substructure finder (Springel et al. 2001) locates gravitationally bound subhalos within each FoF group. For central galaxies, we use the spherical overdensity quantities reported by TNG50 and adopt their 200-times-the-mean–density values as the halo radii and masses for host selection, consistent with the unified definition applied throughout this work.

Satellite subhalos are treated as bound structures within the FoF group. Because SUBFIND does not assign spherical-overdensity radii (e.g. $r_{200\mathrm{m}}$) to satellites, we rely only on their positions, stellar masses, and star formation rates when computing distances from the host and evaluating satellite quenching. No subhalo radius is required for our analysis.

A summary of the numerical characteristics, halo-finding conventions, and stellar-mass definitions used for simulations is provided in Table 1.

Table 1. Summary of the numerical characteristics, halo definitions, and feedback implementations in the three simulation suites analyzed in this work. Each suite retains its halo-finding conventions and stellar-mass definitions. The table lists the dark-matter and baryonic particle masses, spatial resolutions, feedback physics, and the halo and stellar-mass conventions used in FIREbox, the FIRE-2 zoom-ins, and TNG50. These simulation-specific quantities define the physical and numerical context for our comparison to observational datasets.

Property	FIREbox	FIRE-2 zooms	TNG50
Mass resolution, spatial resolution, and feedback			
DM particle mass	$3.3 \times 10^5\, M_\odot$	Isolated: $3.5 \times 10^4\, M_\odot$ Paired: 1.9–$2.0 \times 10^4\, M_\odot$	$4.5 \times 10^5\, M_\odot$
Baryon particle mass	$6.3 \times 10^4\, M_\odot$	Isolated: $7.1 \times 10^3\, M_\odot$ Paired: 3.5–$4.0 \times 10^3\, M_\odot$	$8.5 \times 10^4\, M_\odot$
Spatial resolution	Stars: 12 pc Gas: adaptive to 1.5 pc	Stars: 4 pc Gas: adaptive to 1 pc	Collisionless: 290 pc Gas: adaptive to 74 pc
Feedback channels	SNe Ia/II; stellar winds; photo-ionization; radiation pressure	Same as FIREbox	SNe winds; AGN thermal + kinetic feedback
Halo definitions			
Halo finder	AHF	ROCKSTAR	SUBFIND
$M_{\rm halo}$ definition	$M_{\rm vir} \rightarrow M_{\rm 200m}$	$M_{\rm 200m}$	$M_{\rm 200m}$
$r_{\rm halo}$ definition	$r_{\rm 200m}$	$r_{\rm 200m}$	$r_{\rm 200m}$
Stellar-mass definition	Bound stars within $r^\star_{80}$	Bound stars within $r^\star_{80}$	Total bound stellar mass

2.5. *Observational datasets*

To complement the simulation suites, we incorporate two large observational surveys of Milky Way–mass galaxies: the SAGA and ELVES surveys. Both provide uniform satellite catalogs around statistically significant samples of nearby MW-mass hosts, enabling a direct comparison between synthetic and observed satellite populations in the low-mass regime relevant for quenching studies.

2.5.1. *SAGA: Satellites Around Galactic Analogs*

We use the public Data Release 3 (DR3) from the SAGA Survey[1], which provides photometric and spectroscopic measurements for satellites around 100 Milky Way analogs out to projected distances of 300 kpc (see Mao et al. 2024; Geha et al. 2024). Our analysis focuses on the confirmed and high-probability ("Gold + Silver") satellite samples, corresponding to the DR3 `sample < 3` selection. Host halo masses in SAGA are estimated following the group catalog of Lim et al. (2017), which assigns $M_{\rm halo}$ via abundance matching and group-finding applied to SDSS. For each satellite, DR3 reports stellar masses, Hα equivalent widths, projected separations, and catalog-level quenched classifications. We reconstruct the quenched flag using the DR3 spectroscopic criterion to ensure consistency with the definition used in the SAGA collaboration papers (see Section 2.9).

2.5.2. *ELVES: Exploration of the Local VolumE Satellites*

We also use the compiled ELVES (Greene et al. 2023) satellite catalog released with SAGA Paper IV[2] (Geha et al. 2024), which includes confirmed and candidate satellites around 28 nearby galaxies with K-band luminosities similar to that of the Milky Way. The catalog provides homogenized photometry, distances, stellar masses, quenched classifications, and projected separations for all satellites. Unlike SAGA, this ELVES catalog does not report halo mass estimates for its hosts; we therefore employ ELVES only for satellite-level comparisons and for analyses that do not require host halo masses.

Together, SAGA and ELVES provide complementary observational constraints: SAGA offers a large, statistically uniform sample with probabilistic satellite identification, while ELVES offers deeper coverage of the nearest systems with high-quality stellar population measurements. These datasets serve as key empirical bench-

[1] https://sagasurvey.org/data/

[2] https://github.com/sagasurvey/saga-paper4

marks for evaluating the quenched fraction and structural properties of satellites in our simulated host samples.

2.6. *Stellar-mass definitions*

Because stellar-mass measurements differ across simulations and surveys, we adopt dataset-specific definitions that each capture the total bound stellar mass of a satellite, ensuring physical consistency across all datasets.

For both FIREbox and the FIRE-2 zoom-in simulations, we define the stellar mass of each galaxy as the total mass of all *gravitationally bound* star particles enclosed within the radius $r^{\star}_{80}$, which contains 80% of the bound stellar mass. This choice minimizes sensitivity to tidal debris, optimizes consistency across halo finders (AHF for FIREbox and ROCKSTAR for FIRE-2), and provides a robust measure of the stellar component for low-mass satellites.

For TNG50, we adopt the SUBFIND-reported stellar mass, which corresponds to the total gravitationally bound stellar mass of the subhalo. Because SUBFIND does not assign spherical-overdensity radii to satellites, we use the cataloged bound stellar mass directly without imposing an additional aperture.

For both observational samples, we take the stellar masses provided in the publicly released catalogs. SAGA DR3 stellar masses are derived from optical+UV photometry using SED fitting (see Geha et al. 2024). ELVES stellar masses come from homogeneous optical photometry calibrated to deep imaging of the Local Volume (Greene et al. 2023). We apply no additional aperture corrections or rescaling.

Together, these definitions ensure that stellar masses correspond as closely as possible to the bound stellar components of satellites across all datasets, while respecting the conventions and resolution limits of each simulation suite and survey.

2.7. *Host selection*

To enable consistent comparisons across all datasets, we identify Milky Way–mass hosts using a halo mass range of

$$10^{11.9} \leq M_{\rm halo}/M_{\odot} \leq 10^{12.2}. \quad (2)$$

This interval encompasses the range of recent Milky Way halo-mass estimates derived from stellar kinematics, satellite dynamics, and mass modeling (e.g., Bland-Hawthorn & Gerhard 2016; Watkins et al. 2010; Patel et al. 2017). It also covers the target masses of the FIRE-2 zoom-in simulations, ensuring that all simulated hosts can be treated within a common selection framework.

For FIREbox, the FIRE-2 zooms, and TNG50, we first apply this halo-mass cut to all central galaxies. We then impose the satellite-selection criteria described in Section 2.8. Any central lacking at least one satellite that satisfies the stellar-mass and radial cuts is removed from the final host sample. After all selections, the resulting numbers of Milky Way–mass hosts are 17 for FIREbox, 13 for the FIRE-2 zooms, and 132 for TNG50.

For the SAGA survey, we retain all hosts to preserve statistical power and avoid uncertainties in the cataloged halo-mass estimates. Applying the same halo-mass and satellite cuts used for the simulations would reduce the SAGA sample to 46 hosts, but the corresponding quenched fractions and radial trends are fully consistent with those obtained from the full set. After applying the stellar-mass completeness requirement to SAGA satellites, the final SAGA sample consists of 97 hosts.

For ELVES, we impose two observational cuts. First, we apply a simple absolute-K-band selection,

$$-24.6 \leq M_K \leq -23.0, \quad (3)$$

which approximates the SAGA host-luminosity range and serves as a coarse proxy for Milky Way–mass systems. Second, because many ELVES hosts have imaging and spectroscopy only out to 150–200 kpc, we additionally require a radial coverage of at least 300 kpc, using the cataloged `r_cover` values. This ensures that ELVES hosts are selected on the same physical aperture used for the simulated and SAGA satellite samples. After applying both the K-band and radial-coverage cuts, and enforcing satellite stellar-mass completeness, our final ELVES sample contains 14 hosts.

Figure 1 summarizes the stellar mass–halo mass (SMHM) distributions of the resulting host populations. The systems we include in this figure are those that survive both the halo-mass restriction and the satellite-selection criteria. All simulated hosts lie within the adopted halo-mass interval. However, we include all SAGA hosts to reflect uncertainties in observational halo-mass estimates. The Milky Way and M31 are overplotted as a yellow star and pentagon using $M_{\star,\rm MW} = 5 \times 10^{10}\, M_{\odot}$, $M_{\rm halo,MW} = 10^{12}\, M_{\odot}$, $M_{\star,\rm M31} = 10^{11}\, M_{\odot}$, and $M_{\rm halo,M31} = 2 \times 10^{12}\, M_{\odot}$, values consistent with recent dynamical and stellar-population studies (Flynn et al. 2006; Sick et al. 2015; Tamm et al. 2012; Fardal et al. 2013; Patel et al. 2017; Cautun et al. 2020). The accompanying histograms show the distributions of host stellar mass (right) and halo mass (top), with medians marked by vertical lines matching the colors of each dataset. Because ELVES does not include halo-mass estimates, its hosts appear only in the stellar-mass histogram as the golden line.

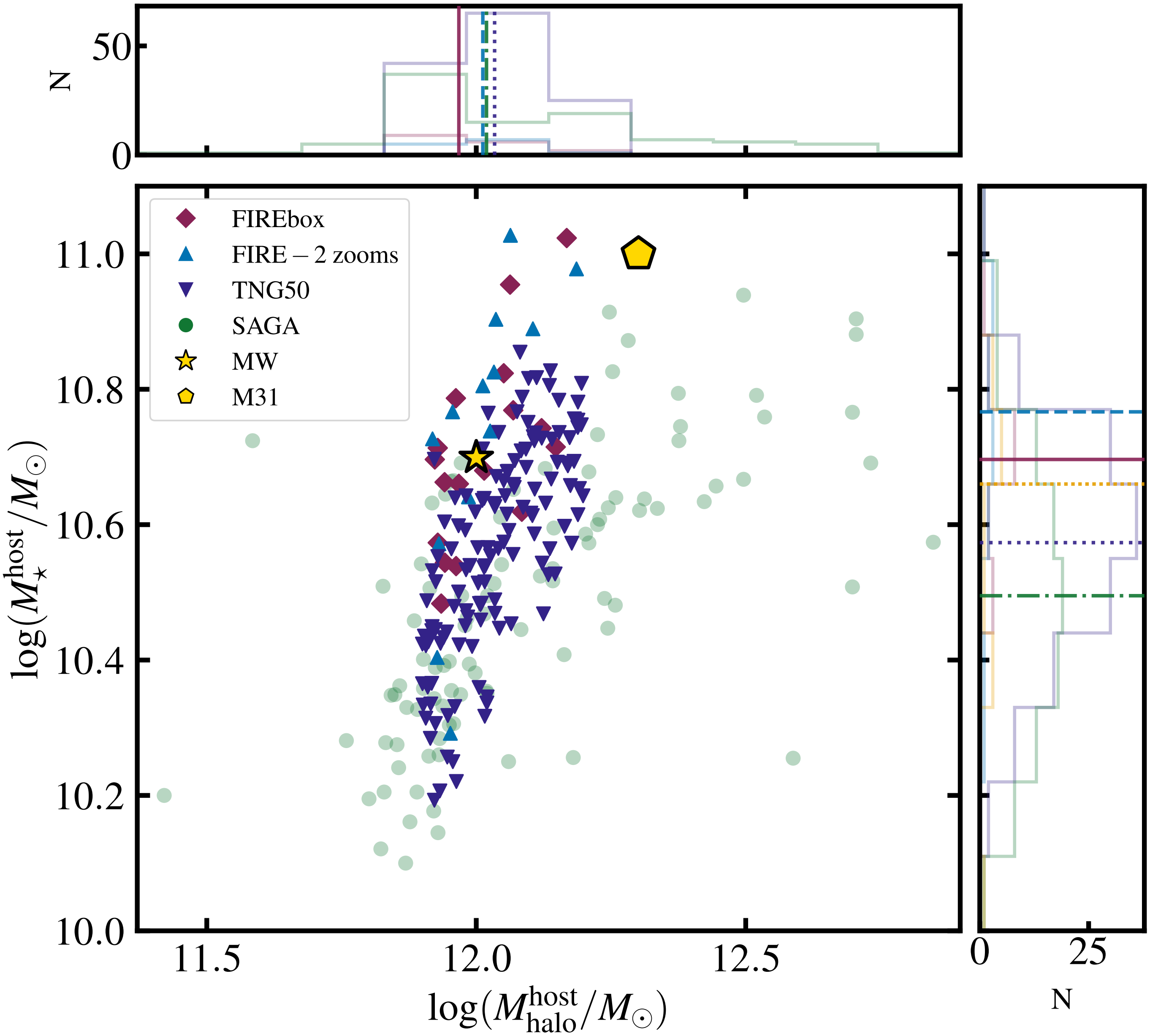

Figure 1. Stellar mass–halo mass (SMHM) relation for host samples drawn from FIREbox (maroon), the FIRE-2 zoom-ins (blue), TNG50 (indigo), and the SAGA survey (green). All simulated hosts lie within the adopted Milky Way–mass range of $10^{11.9} \leq M_{\rm halo}/M_{\odot} \leq 10^{12.2}$, while the full SAGA sample is retained to preserve statistical completeness and account for uncertainties in cataloged halo masses. The Milky Way and M31 are plotted as a yellow star and pentagon using $M_{\star,\rm MW} = 5 \times 10^{10}\,M_{\odot}$, $M_{\rm halo,MW} = 10^{12}\,M_{\odot}$, $M_{\star,\rm M31} = 10^{11}\,M_{\odot}$, and $M_{\rm halo,M31} = 2\times10^{12}\,M_{\odot}$. Histograms of host halo mass (top) and stellar mass (right) share axes with the main panel. All datasets with reported halo masses have medians, $\log_{10}(M_{\rm halo}/M_{\odot}) \sim 12.0$ (FIREbox, FIRE-2 zooms, TNG50, and SAGA). Median stellar masses are $\log_{10}(M_{\star}/M_{\odot}) = 10.7$ (FIREbox), 10.8 (FIRE-2 zooms), 10.6 (TNG50), 10.5 (SAGA), and 10.7 (ELVES). Because ELVES does not provide halo-mass estimates, its hosts appear only in the stellar-mass histogram in golden.

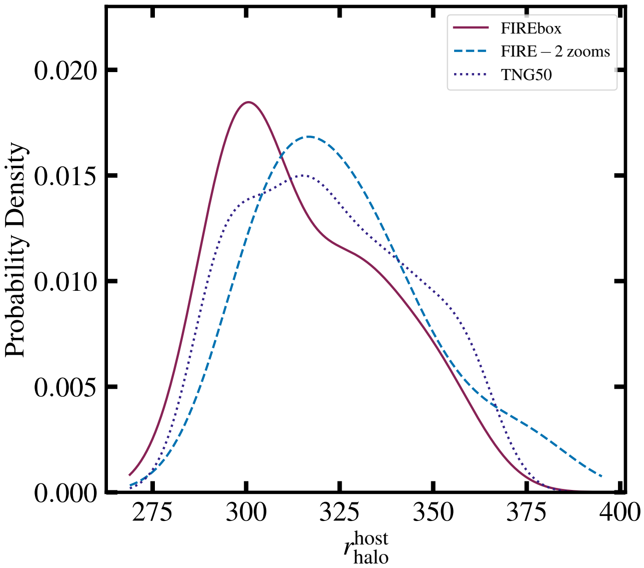

Figure 2. Kernel density estimates of host halo radii, $r_{\rm halo}$, for Milky Way–mass systems drawn from FIREbox (maroon), the FIRE-2 zoom-ins (blue), and TNG50 (indigo). The distributions agree closely, with median radii of 304.6 kpc, 320.3 kpc, and 320.2 kpc, respectively.

Across all datasets, the median stellar masses of the surviving hosts are similar. FIREbox and the FIRE-2 zooms have median stellar masses of $\log_{10}(M_\star/M_\odot) \approx$ 10.7–10.8, while TNG50 hosts have a median of 10.6, SAGA hosts congregate near 10.5, and the ELVES hosts have a median of 10.7. Additionally, all datasets with reported halo masses (FIREbox, the FIRE-2 zooms, TNG50, and the SAGA survey) have median values of $\log_{10}(M_{\rm halo}/M_\odot) \sim 12.0$.

Although the simulations target comparable halo masses, differences in halo-finding methodology introduce small systematic variations in the recovered halo radii. In Figure 2 we show kernel density estimates of the halo radii for each simulation suite, demonstrating that their median radii agree to within approximately twenty kiloparsecs. These offsets motivate our use of fixed physical apertures, both in three dimensions and in projection, when selecting satellites.

2.8. *Satellite selection*

We select satellites uniformly across all datasets using criteria matched to the mass resolution limits and observational completeness thresholds of the SAGA and ELVES surveys. We include all satellites within a three dimensional radius of 300 kpc from the host center and require their stellar masses to lie within

$$7 \leq \log_{10}(M_\star/M_\odot) \leq 10. \tag{4}$$

The lower bound reflects the stellar-mass completeness imposed by the coarsest resolved simulation in our comparison. TNG50 resolves satellites with $M_\star \approx 10^7, M_\odot$ using more than one hundred stellar particles, ensuring that systems above this threshold are well resolved across all three simulation suites. The upper bound excludes unusually massive companions whose stellar masses approach those of Milky Way–mass systems, allowing us to compare satellite populations across simulations and observations using a consistent and conservative definition.

These same stellar mass limits are applied to the observed satellites in both SAGA and ELVES to ensure that all five datasets are compared over a common satellite mass range. After applying all cuts, the final satellite samples contain 25 satellites in FIREbox, 41 in the FIRE-2 zooms, 421 in TNG50, 370 in SAGA, and 88 in ELVES.

The simulations differ in their satellite stellar mass distributions. FIREbox satellites have the highest median stellar mass, $\log_{10}(M_\star/M_\odot) = 8.82$, compared to 7.71 in the FIRE-2 zooms, 7.75 in TNG50, 7.79 in SAGA, and 7.62 in ELVES. These differences likely reflect the varying halo-selection functions, simulation volumes, resolutions, physics implementations, and levels of cosmic variance among the three simulation suites.

For projected analyses, each simulated satellite system is viewed along the XY, XZ, and YZ axes of the simulation box. We exclude atellites with projected distances smaller than 10 kpc or larger than 300 kpc to match the observational selection used in Geha et al. (2024).

2.9. *Quenched classification*

Observational quenching diagnostics rely on tracers of recent star formation such as Hα, UV/FUV continuum, and cold-gas emission (Leroy et al. 2008; Grcevich & Putman 2009; Spekkens et al. 2014; Putman et al. 2021). These indicators probe different characteristic timescales, with Hα tracing star formation over approximately 10 Myr and UV/FUV tracing activity over roughly 100 Myr. Cosmological simulations provide access to the full star formation histories of individual star particles, which allows both time-resolved and observation-matched quiescence definitions (e.g. Akins et al. 2021; Karunakaran et al. 2021). Within the FIRE-2 simulations, Samuel et al. (2022) show that a wide range of quenching definitions produce broadly consistent results for low-mass satellites, supporting the use of simple, observationally motivated thresholds.

For the FIRE simulations, we estimate the SFR using an archaeological method: we sum the mass of all stars formed within the past 10 Myr for stellar particles currently inside the satellite halo radius. This yields a 10 Myr averaged SFR that captures star formation on the timescale probed by Hα in FIRE-2 (Flores Velázquez et al. 2021). We define the specific star formation rate (sSFR) as

$$\mathrm{sSFR}_{z=0} = \frac{\mathrm{SFR}_{10\,\mathrm{Myr}}}{M_{\star}^{\mathrm{sat}}}. \quad (5)$$

We classify satellites as quenched if $\log_{10}(\mathrm{sSFR}_{z=0}) < -11$, consistent with the approximate division used in Geha et al. (2024). For TNG50, we adopt the instantaneous SFR from the public catalog and apply the same threshold.

For the SAGA DR3 dataset, we adopt the primary quenching criterion defined in Geha et al. (2024), which classifies confirmed satellites as quenched when

$$\mathrm{EW}_{\mathrm{H}\alpha} - \sigma_{\mathrm{EW}_{\mathrm{H}\alpha}} < 2\,\text{Å}, \quad (6)$$

where $\mathrm{EW}_{\mathrm{H}\alpha}$ is the Hα equivalent width and $\sigma_{\mathrm{EW}_{\mathrm{H}\alpha}}$ is the associated measurement uncertainty.

Geha et al. (2024) supplement this with a secondary NUV-based sSFR criterion that reclassifies a small number of massive satellites with quenched cores but extended star-forming regions. This adjustment applies only to twelve satellites in their full sample. Because the public DR3 catalog does not include stellar-mass uncertainties needed to reproduce the combined error term in the NUV definition, we do not implement this second step. Given that it affects a very small number of relatively massive satellites, this omission is unlikely to influence our results. For unconfirmed satellites, we adopt the published DR3 quenched flag directly.

For the ELVES sample, we use the quenched flag provided in the compiled catalog from Geha et al. (2024). These classifications are based primarily on optical colors, with supporting UV, Hα, and morphological information where available, as described in Karunakaran et al. (2023). Because ELVES does not provide uniform spectroscopic or UV-based SFR measurements for all satellites, we retain the catalog definitions for consistency with the survey methodology.

3. RESULTS

3.1. *Satellite population comparison*

In Figure 3, we compare the projected radial distributions of satellites across the three simulation suites and the two observational samples. For every dataset, we compute the cumulative fraction of satellites as a function of projected distance and normalize it to the total number of satellites within 300 kpc. For FIREbox (maroon), the FIRE-2 zoom-ins (blue), TNG50 (indigo), SAGA (green), and ELVES (golden), each curve represents the *mean* cumulative radial profile per host, and the shaded regions for the simulations indicate the

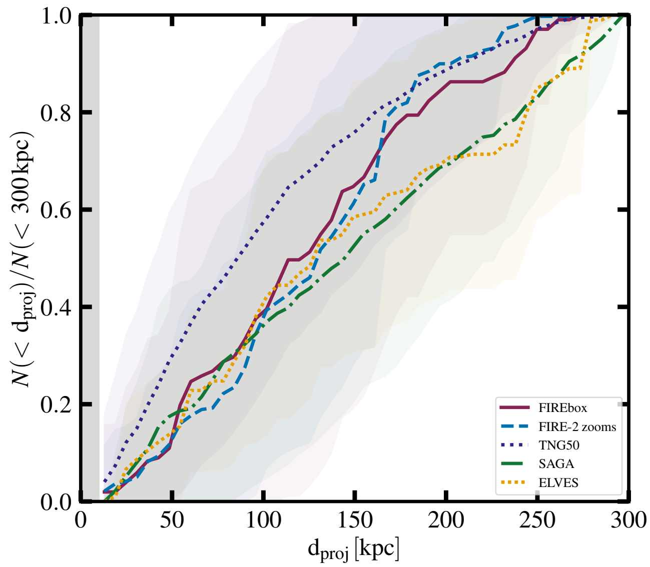

Figure 3. Projected radial distributions of satellites for all five datasets: FIREbox (maroon), FIRE-2 zoom-ins (blue), TNG50 (indigo), SAGA (green), and ELVES (golden). For every dataset, we plot the *mean* cumulative fraction of satellites per host as a function of projected distance, normalized to the number of satellites within 300 kpc. Shaded bands show the 1σ host-to-host scatter for the simulations. Following the SAGA survey strategy, we exclude the inner 10 kpc (gray region), where host-galaxy light severely limits satellite detectability. All five samples exhibit broadly similar radial trends, with only mild differences in the degree of central concentration.

1σ host-to-host scatter. As in the SAGA survey, we exclude the innermost 10 kpc (gray shaded region) because strong contamination from the host galaxy light prevents reliable satellite identification at these radii.

Across most of the 10–300 kpc range, the five samples show broadly similar radial profiles. TNG50 exhibits a modest excess of satellites at smaller radii, producing a slightly more centrally concentrated distribution compared to the other simulation suites and both observational datasets. At projected distances beyond ∼150 kpc, SAGA and ELVES lie mildly below the simulations. Overall, the strong similarity between the five datasets indicates that our fixed-aperture, projected-distance selection provides a robust foundation for cross-suite comparison.

In Figure 4, we compare the stellar cumulative mass functions (SMFs) of satellites across the full sample of simulated and observed hosts. Thin lines show the SMF of each individual host, while the thick curves represent the median SMF for each dataset. The inset histogram displays the distribution of the number of satellites per host, providing a complementary view of the abundance statistics.

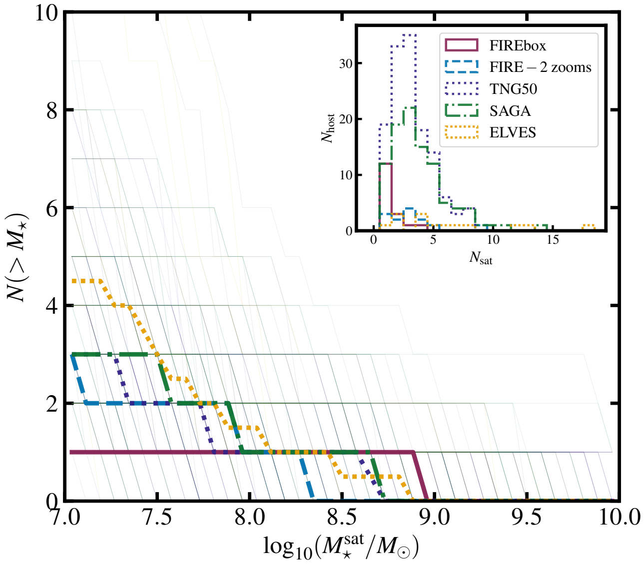

Figure 4. Satellite stellar mass functions (SMFs) for all hosts in FIREbox (maroon), FIRE-2 zoom-ins (blue), TNG50 (indigo), SAGA (green), and ELVES (golden). Thin lines show the SMF for each individual host, while thick lines indicate the median SMF of each dataset. The inset panel shows the distribution of satellite counts per host. The median numbers of satellites in the adopted mass range (10^7–$10^{10}\,M_\odot$) are 1 for FIREbox, 3 for the FIRE-2 zooms and TNG50, 3 for SAGA, and 4.5 for ELVES.

Across all five datasets, the median number of satellites per host remains relatively similar within the stellar-mass range probed here. FIREbox hosts have a median of 1 satellite, whereas the FIRE-2 zoom-ins, TNG50, and SAGA each yield a median of 3. ELVES hosts show a slightly higher median of 4.5 satellites, consistent with their deeper, targeted coverage of the nearby universe. The lower satellite abundance in FIREbox likely reflects a combination of limited volume and sample variance: with only 17 Milky Way–mass hosts drawn from a 22 Mpc box, FIREbox samples fewer environments capable of hosting rich satellite systems, and the intrinsic halo-to-halo scatter at $M_{\rm halo} \sim 10^{12}\,M_\odot$ is large. Differences in halo-finding methodology may also contribute, as AHF can be more conservative in identifying heavily stripped subhalos compared to ROCKSTAR or SUBFIND. Despite these variations, the median stellar-mass functions of the three simulation suites agree well with each other and with both observational samples. This consistency indicates that the adopted stellar-mass range (10^7–$10^{10}\,M_\odot$) yields comparable satellite populations across all datasets and provides a robust foundation for the quenched fraction analysis that follows.

3.2. *Satellite Quenched Fractions*

In Figure 5 we present the satellite quenched fractions for FIREbox, the FIRE-2 zoom-in simulations, and TNG50, compared directly with the SAGA and ELVES surveys and with the combined Milky Way + M31 satellite population from Wetzel et al. (2015). For consistency with the observational literature, we compute all quenched fractions in this work (including those from simulations) as stacked quenched fractions—i.e., the total number of quenched satellites divided by the total number of satellites in each bin. The inclusion of the MW+M31 stacked measurements from Wetzel et al. (2015) provides an additional observational anchor point that reinforces the agreement between the simulations and both survey datasets. We plot Poisson uncertainties for SAGA, ELVES, and all three simulation suites; however, we note that the corresponding host-to-host percentile scatter is typically much larger, often spanning most of the allowable range in quenched fraction (0–1), and therefore represents the dominant source of intrinsic variation.

In the left panel we show the quenched fraction as a function of satellite stellar mass. Across all three simulation suites, the quenched fraction increases sharply toward lower stellar mass, in excellent quantitative agreement with SAGA, ELVES, and the Local Group. The inclusion of the MW+M31 stacked measurements, adapted from Wetzel et al. (2015), provides a useful additional dataset and further confirms the remarkable consistency between the observed and simulated stellar-mass trends. FIREbox predicts somewhat higher quenched fractions over part of the mass range, but these differences remain within the (often substantial) Poisson uncertainties. TNG50 and the FIRE-2 zoom-ins more closely track the MW+M31 points and the two survey datasets.

In the right panel, we show the quenched fraction as a function of projected distance from the host. For the simulation suites, we incorporate all three orthogonal sightline orientations discussed in Section 2.8, treating each as an independent projection to improve statistical robustness and to mirror the line-of-sight projection inherent to observational samples. The SAGA and ELVES datasets exhibit a gently declining quenched fraction with radius: environmental quenching is strongest inside ~50–100 kpc and weakens outward. Among the simulations, TNG50 best reproduces this gradual decline. FIREbox displays a nearly flat trend that remains statistically consistent with the observations once uncertainties are considered. The FIRE-2 zoom-ins depart more noticeably at small radii, showing a suppressed quenched fraction inside ~ 50 kpc. As demonstrated in Section 3.3, this behavior arises from the paired FIRE-2

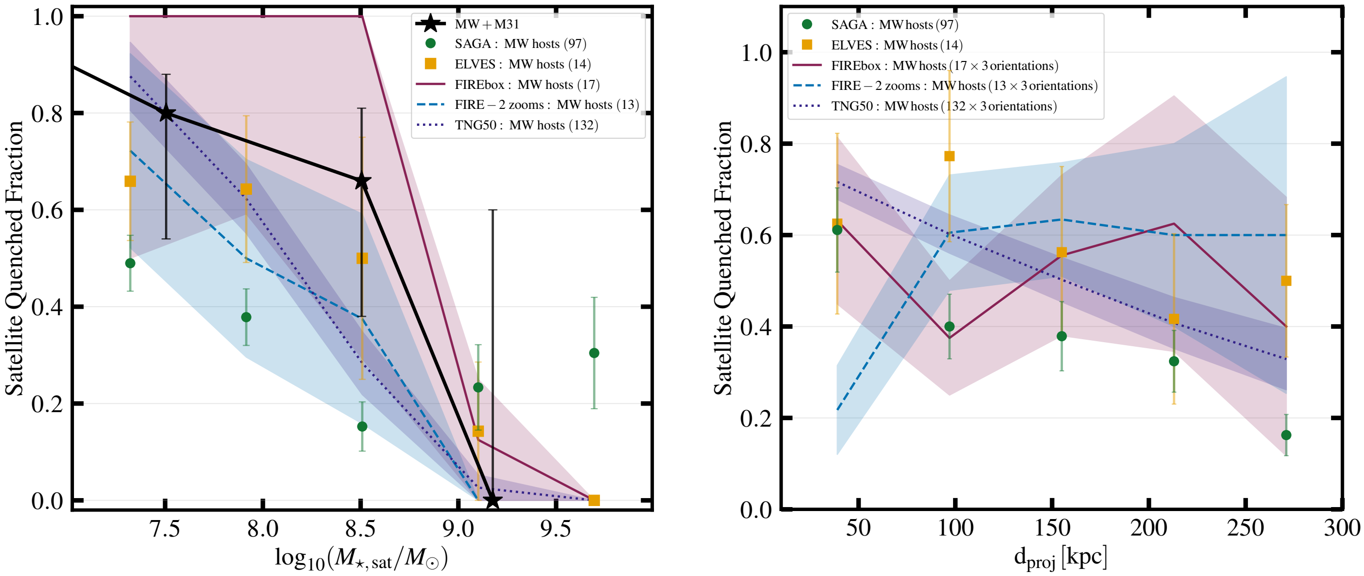

Figure 5. Satellite quenched fractions as a function of stellar mass (left) and projected distance from the host (right). Green circles and golden squares show measurements from the SAGA and ELVES surveys with Poisson uncertainties, and black stars mark the stacked quenched fractions of the combined Milky Way + M31 satellite sample from Wetzel et al. (2015), with error bars giving the 68% confidence interval. Simulation predictions from FIREbox (maroon), the FIRE-2 zoom-ins (blue), and TNG50 (indigo) are shown with shaded regions representing Poisson uncertainties on the stacked quenched fractions; for the radial trends, the simulation curves incorporate all three orthogonal sightline projections discussed in Section 2.8. All three simulation suites successfully reproduce the strong rise in quenched fraction toward low stellar masses, in excellent agreement with SAGA, ELVES, and the Local Group hosts. Radial trends show greater diversity: TNG50 closely matches the observed gradual decline with projected distance, FIREbox remains statistically consistent with a nearly flat profile once uncertainties are considered, and the FIRE-2 zoom-ins exhibit a suppressed quenched fraction at small radii (~ 50 kpc), a behavior traced in Section 3.3 to the paired FIRE-2 host systems.

systems, whose satellite populations drive the unexpectedly low central quenched fractions.

Overall, the stellar-mass dependence of satellite quenching shows strikingly good agreement across all three simulation suites and all three observational samples (including MW+M31), indicating that this trend is a robust outcome of contemporary galaxy-formation models despite their differing volumes, physics implementations, and numerical resolutions. The radial trends, by contrast, are more sensitive to host-halo conditions and to the modeling of environmental processes, and therefore provide a powerful diagnostic for understanding the mechanisms that drive satellite quenching.

3.3. *Environmental dependence in the FIRE-2 zoom-ins*

The FIRE-2 zoom-ins display the strongest discrepancy among the simulations in their radial quenched fraction trends (Section 3.2). To investigate the origin of this behavior, we divide the FIRE-2 hosts into isolated Milky Way analogs and paired MW–M31 analogs. In Figure 6 we compare the quenched fractions for satellites around these two subsets as a function of both satellite stellar mass (left) and projected host-centric distance (right).

In the stellar-mass panel, paired systems (orange) lack satellites above $M_\star \approx 10^{8.5}\,M_\odot$, whereas isolated hosts (blue) retain satellites extending to $M_\star \gtrsim 10^9\,M_\odot$. Samuel et al. (2022) present a similar comparison in their Fig. 5 and likewise report that the paired systems host fewer massive satellites, although their exact trends differ because they use a stricter quenching threshold and include satellites down to lower stellar masses.

The radial trends show an even sharper contrast. Satellites of isolated hosts follow the familiar pattern of strong central quenching, consistent with SAGA, ELVES, FIREbox, and TNG50. Satellites of the paired hosts, however, show the opposite behavior: the quenched fraction is *lowest* at small projected radii and increases toward larger distances. This inverted trend directly reproduces the discrepancy highlighted in Figure 5 and confirms that the paired systems drive the suppressed inner quenched fractions in the FIRE-2 suite.

To explore the origin of this behavior, we examine satellite properties as a function of their 3D host-centric distances in Figure 7. We display satellites around paired hosts in the top row and those around isolated hosts the bottom row. Star-forming satellites appear as orange circles and quenched satellites as red trian-

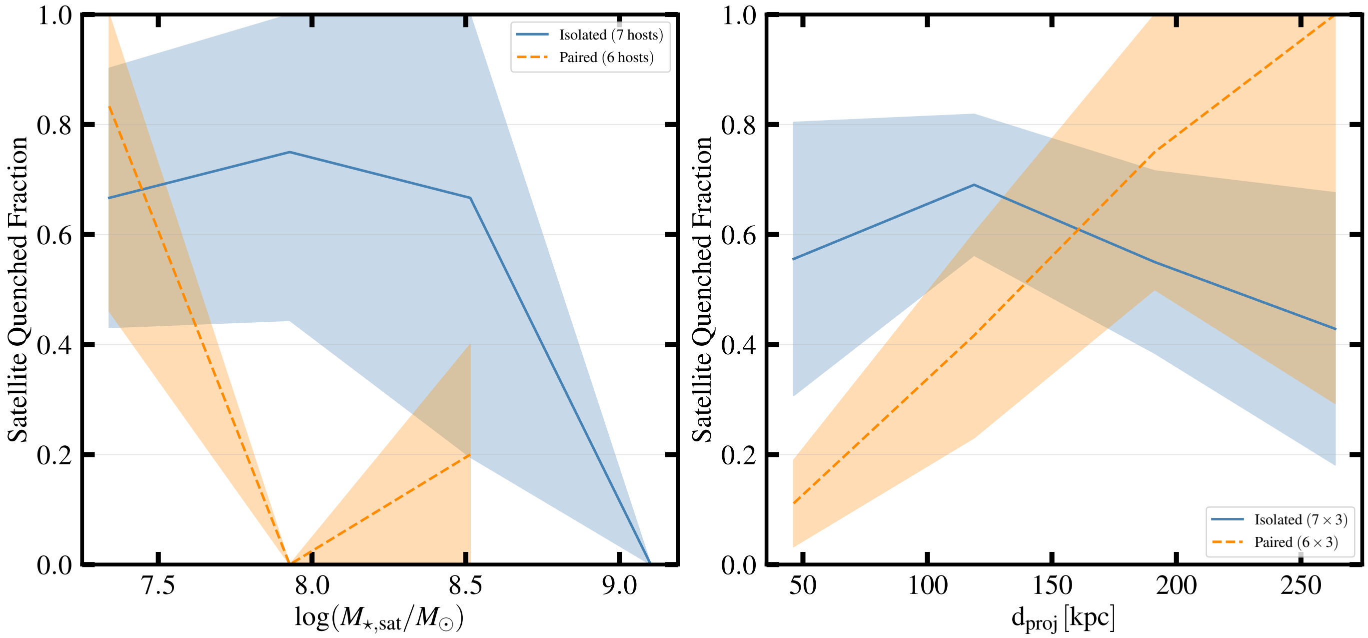

Figure 6. Satellite quenched fractions in the FIRE-2 zoom-ins split by host environment: isolated MW analogs (blue) and paired MW–M31 analogs (orange). *Left:* As a function of satellite stellar mass, paired hosts lack satellites more massive than $M_\star \approx 10^{8.5}\,M_\odot$, indicating a distinct satellite mass distribution compared to the isolated systems. *Right:* As a function of projected distance, satellites of paired hosts show a rising quenched fraction with increasing $d_{\rm proj}$, opposite to the strong central quenching seen in the isolated FIRE-2 hosts, the simulations in Figure 5, and both observed samples (SAGA and ELVES). This reversal suggests that the paired systems drive the discrepancy in the FIRE-2 radial trend.

gles; we adopt $\mathrm{sSFR}_{10\,\mathrm{Myr}} = 10^{-11}\,\mathrm{yr}^{-1}$ for all quenched satellites.

Two trends stand out. First, satellites of the paired hosts show strong segregation: star-forming satellites concentrate at small radii and higher stellar masses, while quenched satellites are predominantly lower mass and occupy the outskirts. Second, the isolated hosts show a more mixed and more massive satellite population, spanning a broad range in both $M_\star$ and r_{3D} and hosting significantly more satellites above our adopted completeness limit.

These results demonstrate that the FIRE-2 paired systems differ markedly from isolated systems in both satellite abundance and satellite mass distribution. Their lack of high-mass satellites and strong radial segregation between star-forming and quenched satellites naturally produce the unusual quenched fraction profile seen in Figure 5. These differences may reflect variations in assembly history or environmental preprocessing, but a definitive interpretation requires an analysis of satellite orbits, infall times, and gas histories. We will pursue this in a follow-up study focused on the environmental pathways of satellite quenching.

4. DISCUSSION

4.1. *Implications of our results*

Comparing satellite populations across simulations presents several challenges, even when host mass ranges and selection criteria are carefully matched. Differences in halo-finding algorithms, numerical resolution, and feedback implementations each introduce systematic variations that complicate direct comparisons. These differences affect both the inferred properties of halos and the resulting star formation histories of their satellites.

Despite these challenges, our results show that the *mass dependence* of satellite quenching is a robust predictions of contemporary galaxy-formation models. All three simulation suites reproduce the strong trend that lower-mass satellites are more likely to be quenched (Figure 5, left panel), in excellent qualitative agreement with observations. This consistency suggests that the essential coupling between stellar feedback, gas removal, and environmental processes is broadly captured across very different numerical frameworks.

By contrast, the *radial* quenched fraction trends respond sensitively to the physical conditions of the host halo and to the modeling of environmental processes. Here the FIRE-2 zoom-ins diverge most strongly from the observations and the other simulations. We show in Section 3.3 that this behavior originates entirely from the paired FIRE-2 systems, whose satellite populations differ markedly from their isolated counterparts. The

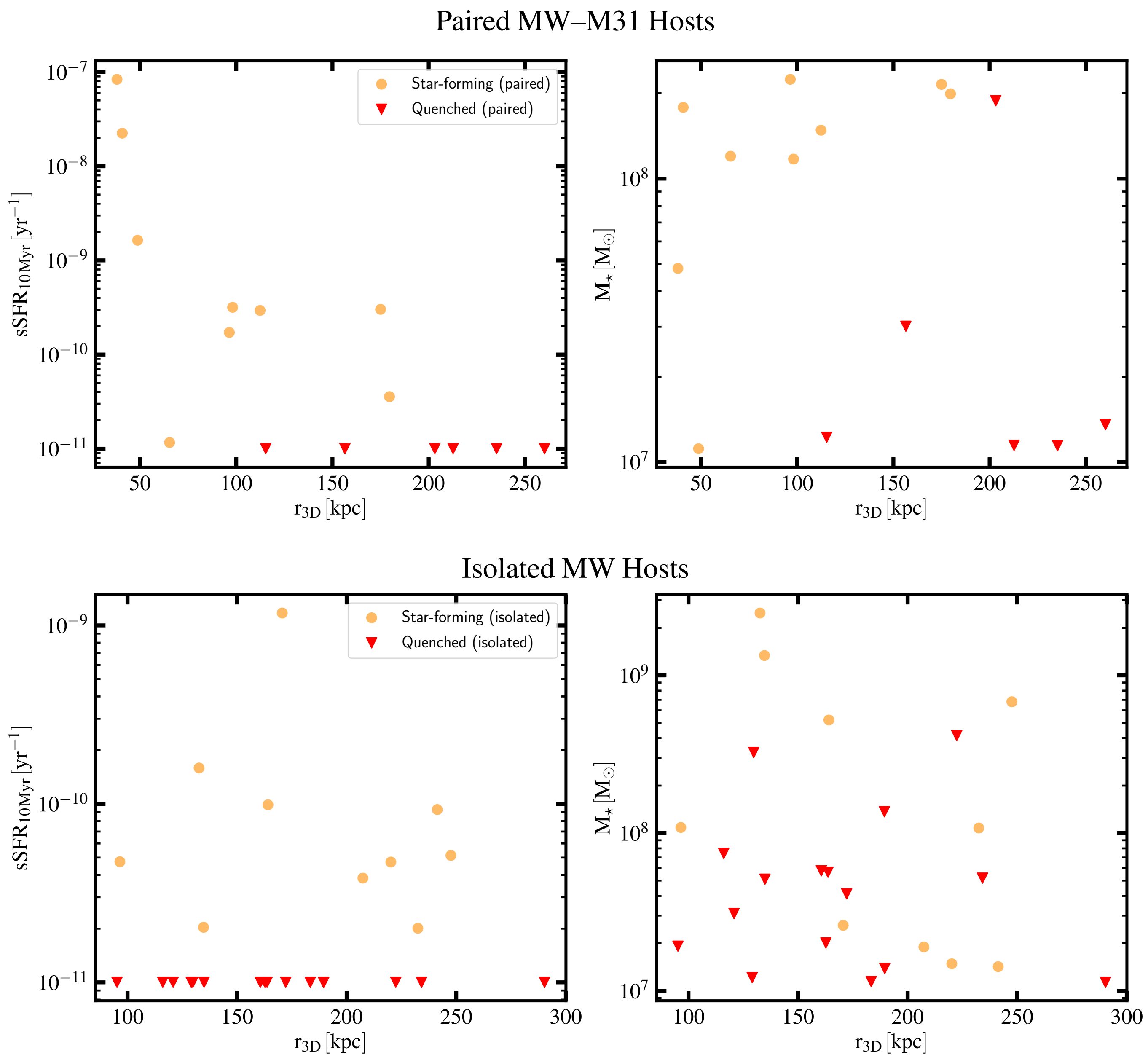

Figure 7. Structural properties of satellites in the FIRE-2 zoom-ins, separated by host environment. *Top:* Satellites of the paired MW–M31 analogs. Star-forming satellites (orange circles) are both closer to their hosts and more massive, while quenched satellites (red triangles) occupy larger radii and lower stellar masses. *Bottom:* Satellites of the isolated MW analogs. Star-forming and quenched satellites span a wider range of distances and masses, including satellites as massive as $M_\star \sim 3 \times 10^9\, M_\odot$, and the isolated hosts contain more satellites above our completeness threshold of $M_\star > 10^7\, M_\odot$. These structural differences underlie the divergent quenched fraction trends seen in Figure 6.

paired hosts lack massive satellites, show strong radial segregation between star-forming and quenched systems, and ultimately produce an inverted quenched fraction profile in which the lowest quenched fractions occur at the smallest radii.

These results underscore the possibility that a host's *own* environment can imprint itself on the quenched fractions of its satellites. Because we impose no strong isolation criteria on MW-mass hosts in FIREbox or TNG50–beyond requiring that they be centrals–any analogous signal in those suites may be diluted by statistical mixing across a wide range of environments. This caveat motivates a more systematic, controlled investigation of host environment and assembly history in future work.

Host properties themselves likely play a key role in shaping satellite quenching. The SAGA survey shows that more massive hosts tend to have higher quenched fractions among their lowest-mass satellites, suggesting a mass-dependent influence on environmental processing (Geha et al. 2024). Martín-Navarro et al. (2021) further argue that AGN activity can potentially enhance quenching anisotropically, preferentially affecting satellites along the axis of a black hole jet. Such results emphasize the need to examine how host-specific factors (for example, stellar mass, black hole accretion rate, AGN luminosity, and feedback morphology) modulate the quenching efficiency of surrounding satellites.

It is also important to consider how representative the simulation suites are of the broader galaxy population. FIREbox, while high resolution, spans a modest cosmological volume and may under-sample rare environments. The FIRE-2 zoom-ins are selected to be MW-mass halos that are isolated from comparably massive neighbors but are not tailored to reproduce detailed Milky Way or Local Group properties; several of the zoom-ins lack massive satellites such as the LMC or M33. These limitations reinforce the need to disentangle internal physics, host properties, and large-scale environment when interpreting quenching trends.

4.2. *Additional factors not explored in this work*

Several physical ingredients relevant to satellite quenching lie beyond the scope of the present analysis. One is the detailed gas content of satellites. Previous work shows that most satellites within the virial radius of MW-like hosts are gas poor, having been stripped of their gas after infall, while the low-mass galaxies that retain significant gas are generally isolated systems (Simpson et al. 2018; Samuel et al. 2022; Engler et al. 2023). Akins et al. (2021) find that quenching timescales correlate positively with gas mass at infall, suggesting that gas-rich satellites can remain star forming long after entering a host halo.

Another consideration is how observational selection effects shape the inferred quenched fractions. Interlopers, projection effects, and surface-brightness limits can all bias satellite samples, especially at large projected radii where star-forming interlopers may artificially suppress the measured quenched fraction. Mock survey analyses constructed from the simulations will be important for quantifying these effects and assessing how observational limitations contribute to differences between the simulations and the SAGA and ELVES datasets.

Work at other host mass scales also provides broader context. Observational and simulation studies explore quenched fractions around lower-mass hosts (e.g., Jahn et al. 2022; Li et al. 2025) and around group- and cluster-scale systems (e.g., Donnari et al. 2021; Baxter et al. 2021). These studies show that the efficiency and dominant mechanisms of quenching vary significantly with host mass, suggesting that satellite quenching reflects a continuum of environmental processes operating across halo scales. Integrating insights across these regimes will be important for constructing a unified view of low-mass galaxy quenching.

4.3. *Future directions*

Two forthcoming projects led by the present author will directly extend the analysis presented here. The first (Mercado et al. 2026a, in prep) will isolate the role of host environment by examining how satellite quenched fractions vary across isolated, paired, and group-like systems in FIRE-2, FIREbox, and TNG50. The second (Mercado et al. 2026b, in prep) will investigate how host properties, including stellar mass, CGM structure, and black hole activity, modulate the quenching efficiency of low-mass satellites.

These efforts will proceed in parallel with two complementary studies within the FIRE collaboration. A detailed analysis of satellite orbits, infall times, and gas histories in the FIRE-2 zoom-ins (Gogliettino & Gandhi et al., in prep) will quantify the connection between assembly history, environmental preprocessing, and the structural segregation identified in Section 3.3. A second study using FIREbox together with a subset of FIRE-2 zoom-ins (Tortora et al., in prep) will construct full mock observations to evaluate selection effects and to assess how faithfully simulated satellites can be compared to systems identified in surveys such as SAGA and ELVES.

Together, these projects will establish a broader framework in which both *nature* (internal galaxy physics) and *nurture* (environment and assembly history) jointly regulate the quenching pathways of low-mass satellites around Milky Way–mass galaxies.

5. SUMMARY AND CONCLUSIONS

In this work, we compare satellite populations across three state-of-the-art cosmological simulation suites (FIREbox, the FIRE 2 zoom-ins, and TNG50), two large observational datasets (SAGA and ELVES), and the combined MW plus M31 satellite population. By applying nearly consistent host and satellite selection criteria, along with common quenching definitions, we examine how well contemporary galaxy-formation models reproduce the observed dependencies of satellite quenching on stellar mass and projected host distance.

Our main conclusions are as follows:

- **Mass dependence of quenching is robust.** All three simulation suites reproduce the strong empirical trend that lower-mass satellites are more likely to be quenched. This agreement extends across the SAGA and ELVES surveys and the combined MW plus M31 sample, indicating that the simulations capture the same mass-dependent behavior seen in the full set of available observations. Despite substantial differences in numerical resolution, halo-finding methodology, and feedback modeling, the consistency across both simulations and observations demonstrates that the mass dependence of satellite quenching is a robust outcome of contemporary galaxy-formation models.

- **Radial quenched fraction trends broadly agree, with notable discrepancies linked to host environment and halo physics.** Observations from SAGA and ELVES show gently declining quenched fractions with projected distance, reflecting strong environmental quenching at small radii. All three simulation suites qualitatively reproduce either weak or mildly falling radial trends within their uncertainties, but meaningful differences arise in the details: TNG50 most closely matches the observed decline, FIREbox is consistent with only modest radial variation across the probed range, and the FIRE-2 zoom-ins show suppressed inner quenched fractions driven entirely by their paired MW–M31 analogs. These variations may reflect differences in host-halo conditions (for example, circumgalactic medium structure, gas-removal efficiency, or feedback processes) as well as the imprint of host environment and assembly history.

- **The discrepancy in FIRE-2 originates entirely from the paired MW–M31 analogs.** Splitting the FIRE-2 hosts into isolated and paired systems reveals that only the paired hosts exhibit the inverted radial trend. These paired systems lack high-mass satellites, show strong radial segregation between star-forming and quenched satellites, and produce quenched fractions that *increase* with projected distance. Isolated FIRE-2 hosts, by contrast, show the expected strong central quenching. This result identifies a previously unrecognized environmental imprint within the FIRE-2 suite and demonstrates that host environment can strongly modulate satellite quenching outcomes.

- **Host environment may contribute to the diversity of radial quenching trends.** The FIRE-2 paired systems display distinct satellite populations and quenched fraction profiles compared to their isolated counterparts, suggesting that a host's larger-scale environment or assembly history can leave an imprint on its satellites. In FIREbox and TNG50, where MW-mass centrals occupy a broad range of larger-scale environments, any such effects may be averaged out. While the present analysis cannot fully quantify this dependence, the results highlight the importance of exploring host environment and assembly history in a more systematic way.

- **Satellite populations are broadly similar across datasets in number and stellar mass.** Across FIREbox, FIRE-2, TNG50, SAGA, and ELVES, the stellar mass functions and projected radial distributions of satellites show strong agreement. Median satellite counts per host differ only modestly across datasets, supporting the validity of comparing quenched fractions within a unified stellar-mass range of 10^7–$10^{10}\ M_\odot$.

- **Interpretation requires caution due to observational and numerical systematics.** Differences in halo finders, simulation volumes, resolution limits, and observational selection functions each introduce systematic uncertainties. Forward modeling (i.e. including projection effects, interlopers, and surface-brightness limitations-) will be essential for quantitative comparisons.

Taken together, our results demonstrate that while contemporary simulations successfully reproduce the mass dependence of satellite quenching, they can diverge markedly in their radial trends. The behavior of the FIRE-2 paired systems highlights that host environment and assembly history can imprint strongly on satellite quenching statistics. This finding motivates more systematic studies of host environment across all simulation suites and reinforces the need for careful forward modeling when comparing simulations with observations.

Two companion studies led by the present author will build directly on these results by quantifying how both host environment and host properties regulate satellite quenching across FIRE-2, FIREbox, and TNG50. Together with complementary work in the FIRE collaboration, these efforts aim to establish a unified framework in which both *Nature* (internal galaxy physics) and *Nurture* (environment and assembly history) jointly shape the quenching pathways of low-mass satellites around Milky Way–mass galaxies.

ACKNOWLEDGMENTS

FJM is funded by the National Science Foundation (NSF) Math and Physical Sciences (MPS) Award AST-2316748. DCB is supported by an NSF Astronomy and Astrophysics Postdoctoral Fellowship under award AST-2303800 as well as by the Chancellor's Postdoctoral Fellowship. MKRW acknowledges support from NSF MPS Ascending Faculty Catalyst Award AST-2444751. JM is funded by a Pomona College Large Research Grant. received support from NSF, via CAREER award AST-2045928 and grant AST-2107772.

Software: The functionalities provided by the following python packages played a critical role in the analysis and visualizations presented in this paper: **matplotlib** (Hunter 2007), **NumPy** (Van Der Walt et al. 2011), **SciPy** (Virtanen et al. 2020) and **iPython** (Perez & Granger 2007).

REFERENCES

Akins, H. B., Christensen, C. R., Brooks, A. M., et al. 2021, ApJ, 909, 139, doi: 10.3847/1538-4357/abe2ab

Baxter, D. C., Cooper, M. C., & Fillingham, S. P. 2021, MNRAS, 503, 1636, doi: 10.1093/mnras/stab523

Behroozi, P. S., Wechsler, R. H., & Wu, H.-Y. 2013, ApJ, 762, 109, doi: 10.1088/0004-637X/762/2/109

Benavides, J. A., Sales, L. V., Wetzel, A., et al. 2025, MNRAS, doi: 10.1093/mnras/staf1847

Bland-Hawthorn, J., & Gerhard, O. 2016, ARA&A, 54, 529, doi: 10.1146/annurev-astro-081915-023441

Brown, T. M., Tumlinson, J., Geha, M., et al. 2014, ApJ, 796, 91, doi: 10.1088/0004-637X/796/2/91

Bryan, G. L., & Norman, M. L. 1998, ApJ, 495, 80, doi: 10.1086/305262

Bullock, J. S., Kolatt, T. S., Sigad, Y., et al. 2001, MNRAS, 321, 559, doi: 10.1046/j.1365-8711.2001.04068.x

Carleton, T., Ellsworth-Bowers, T., Windhorst, R. A., et al. 2024, ApJL, 961, L37, doi: 10.3847/2041-8213/ad1b56

Carlsten, S. G., Greene, J. E., Beaton, R. L., Danieli, S., & Greco, J. P. 2022, ApJ, 933, 47, doi: 10.3847/1538-4357/ac6fd7

Carlsten, S. G., Greene, J. E., Greco, J. P., Beaton, R. L., & Kado-Fong, E. 2021, ApJ, 922, 267, doi: 10.3847/1538-4357/ac2581

Cautun, M., Benítez-Llambay, A., Deason, A. J., et al. 2020, MNRAS, 494, 4291, doi: 10.1093/mnras/staa1017

Christensen, C. R., Brooks, A. M., Munshi, F., et al. 2024, ApJ, 961, 236, doi: 10.3847/1538-4357/ad0c5a

Davis, M., Efstathiou, G., Frenk, C. S., & White, S. D. M. 1985, ApJ, 292, 371, doi: 10.1086/163168

Donnari, M., Pillepich, A., Nelson, D., et al. 2021, MNRAS, 506, 4760, doi: 10.1093/mnras/stab1950

Engler, C., Pillepich, A., Joshi, G. D., et al. 2023, MNRAS, 522, 5946, doi: 10.1093/mnras/stad1357

Fardal, M. A., Weinberg, M. D., Babul, A., et al. 2013, MNRAS, 434, 2779, doi: 10.1093/mnras/stt1121

Faucher-Giguère, C.-A., Lidz, A., Zaldarriaga, M., & Hernquist, L. 2009, ApJ, 703, 1416, doi: 10.1088/0004-637X/703/2/1416

Feldmann, R., Quataert, E., Faucher-Giguère, C.-A., et al. 2023, MNRAS, 522, 3831, doi: 10.1093/mnras/stad1205

Fillingham, S. P., Cooper, M. C., Kelley, T., et al. 2019, arXiv e-prints, arXiv:1906.04180, doi: 10.48550/arXiv.1906.04180

Flores Velázquez, J. A., Gurvich, A. B., Faucher-Giguère, C.-A., et al. 2021, MNRAS, 501, 4812, doi: 10.1093/mnras/staa3893

Flynn, C., Holmberg, J., Portinari, L., Fuchs, B., & Jahreiß, H. 2006, MNRAS, 372, 1149, doi: 10.1111/j.1365-2966.2006.10911.x

Font, A. S., McCarthy, I. G., Belokurov, V., Brown, S. T., & Stafford, S. G. 2022, MNRAS, 511, 1544, doi: 10.1093/mnras/stac183

Garrison-Kimmel, S., Wetzel, A., Bullock, J. S., et al. 2017, MNRAS, 471, 1709, doi: 10.1093/mnras/stx1710

Garrison-Kimmel, S., Hopkins, P. F., Wetzel, A., et al. 2019a, MNRAS, 487, 1380, doi: 10.1093/mnras/stz1317

Garrison-Kimmel, S., Wetzel, A., Hopkins, P. F., et al. 2019b, MNRAS, 489, 4574, doi: 10.1093/mnras/stz2507

Geha, M., Blanton, M. R., Yan, R., & Tinker, J. L. 2012, ApJ, 757, 85, doi: 10.1088/0004-637X/757/1/85

Geha, M., Wechsler, R. H., Mao, Y.-Y., et al. 2017, ApJ, 847, 4, doi: 10.3847/1538-4357/aa8626

Geha, M., Mao, Y.-Y., Wechsler, R. H., et al. 2024, ApJ, 976, 118, doi: 10.3847/1538-4357/ad61e7

Giovanelli, R., Haynes, M. P., Adams, E. A. K., et al. 2013, AJ, 146, 15, doi: 10.1088/0004-6256/146/1/15

Grcevich, J., & Putman, M. E. 2009, ApJ, 696, 385, doi: 10.1088/0004-637X/696/1/385

Greene, J. E., Danieli, S., Carlsten, S., et al. 2023, ApJ, 949, 94, doi: 10.3847/1538-4357/acc58c

Hahn, O., & Abel, T. 2011, MNRAS, 415, 2101, doi: 10.1111/j.1365-2966.2011.18820.x

Hopkins, P. F. 2015, MNRAS, 450, 53, doi: 10.1093/mnras/stv195

Hopkins, P. F., Wetzel, A., Kereš, D., et al. 2018, MNRAS, 480, 800, doi: 10.1093/mnras/sty1690

Hunter, J. D. 2007, Computing in Science and Engineering, 9, 90, doi: 10.1109/MCSE.2007.55

Jahn, E. D., Sales, L. V., Wetzel, A., et al. 2022, MNRAS, 513, 2673, doi: 10.1093/mnras/stac811

Jones, M. G., Sand, D. J., Mutlu-Pakdil, B., et al. 2024, ApJL, 971, L37, doi: 10.3847/2041-8213/ad676e

Karunakaran, A., Sand, D. J., Jones, M. G., et al. 2023, MNRAS, 524, 5314, doi: 10.1093/mnras/stad2208

Karunakaran, A., Spekkens, K., Oman, K. A., et al. 2021, ApJL, 916, L19, doi: 10.3847/2041-8213/ac0e3a

Klein, C., Bullock, J. S., Xia, L., et al. 2025, arXiv e-prints, arXiv:2503.05612, doi: 10.48550/arXiv.2503.05612

Knollmann, S. R., & Knebe, A. 2009, ApJS, 182, 608, doi: 10.1088/0067-0049/182/2/608

Kroupa, P. 2002, Science, 295, 82, doi: 10.1126/science.1067524

Leitherer, C., Schaerer, D., Goldader, J. D., et al. 1999, ApJS, 123, 3, doi: 10.1086/313233

Leroy, A. K., Walter, F., Brinks, E., et al. 2008, AJ, 136, 2782, doi: 10.1088/0004-6256/136/6/2782

Li, J., Greene, J. E., Carlsten, S. G., & Danieli, S. 2024, ApJL, 975, L23, doi: 10.3847/2041-8213/ad5b59

Li, J., Greene, J. E., Danieli, S., et al. 2025, arXiv e-prints, arXiv:2504.08030, doi: 10.48550/arXiv.2504.08030

Lim, S. H., Mo, H. J., Lu, Y., Wang, H., & Yang, X. 2017, MNRAS, 470, 2982, doi: 10.1093/mnras/stx1462

Ma, X., Hopkins, P. F., Wetzel, A. R., et al. 2017, MNRAS, 467, 2430, doi: 10.1093/mnras/stx273

Mancera Piña, P. E., Read, J. I., Kim, S., et al. 2025, A&A, 699, A311, doi: 10.1051/0004-6361/202554381

Mao, Y.-Y., Geha, M., Wechsler, R. H., et al. 2021, ApJ, 907, 85, doi: 10.3847/1538-4357/abce58

—. 2024, ApJ, 976, 117, doi: 10.3847/1538-4357/ad64c4

Martín-Navarro, I., Pillepich, A., Nelson, D., et al. 2021, Nature, 594, 187, doi: 10.1038/s41586-021-03545-9

McCluskey, F., Wetzel, A., Loebman, S. R., et al. 2024, MNRAS, 527, 6926, doi: 10.1093/mnras/stad3547

McQuinn, K. B. W., Newman, M. J. B., Skillman, E. D., et al. 2024, ApJ, 976, 60, doi: 10.3847/1538-4357/ad8158

Meng, J., Li, C., Mo, H. J., et al. 2023, ApJ, 944, 75, doi: 10.3847/1538-4357/acae86

Mercado, F. J., Moreno, J., Feldmann, R., et al. 2025, ApJ, 983, 93, doi: 10.3847/1538-4357/adbf07

Moreno, J., Wheeler, C., Mercado, F. J., et al. 2025, arXiv e-prints, arXiv:2511.03785, doi: 10.48550/arXiv.2511.03785

Mutlu-Pakdil, B., Jones, M. G., Sand, D. J., et al. 2025, arXiv e-prints, arXiv:2509.16307, doi: 10.48550/arXiv.2509.16307

Nadler, E. O., Wechsler, R. H., Bechtol, K., et al. 2020, ApJ, 893, 48, doi: 10.3847/1538-4357/ab846a

Nelson, D., Pillepich, A., Springel, V., et al. 2018a, MNRAS, 475, 624, doi: 10.1093/mnras/stx3040

—. 2018b, MNRAS, 475, 624, doi: 10.1093/mnras/stx3040

Patel, E., Besla, G., & Mandel, K. 2017, MNRAS, 468, 3428, doi: 10.1093/mnras/stx698

Perez, F., & Granger, B. E. 2007, Computing in Science and Engineering, 9, 21, doi: 10.1109/MCSE.2007.53

Pillepich, A., Springel, V., Nelson, D., et al. 2018a, MNRAS, 473, 4077, doi: 10.1093/mnras/stx2656

Pillepich, A., Nelson, D., Hernquist, L., et al. 2018b, MNRAS, 475, 648, doi: 10.1093/mnras/stx3112

Planck Collaboration, Ade, P. A. R., Aghanim, N., et al. 2016, A&A, 594, A13, doi: 10.1051/0004-6361/201525830

Putman, M. E., Zheng, Y., Price-Whelan, A. M., et al. 2021, ApJ, 913, 53, doi: 10.3847/1538-4357/abe391

Rodríguez-Cardoso, R., Roca-Fàbrega, S., Jung, M., et al. 2025, A&A, 698, A303, doi: 10.1051/0004-6361/202453639

Rodriguez Wimberly, M. K., Cooper, M. C., Fillingham, S. P., et al. 2019, MNRAS, 483, 4031, doi: 10.1093/mnras/sty3357

Samuel, J., Wetzel, A., Santistevan, I., et al. 2022, MNRAS, 514, 5276, doi: 10.1093/mnras/stac1706

Samuel, J., Wetzel, A., Tollerud, E., et al. 2020, MNRAS, 491, 1471, doi: 10.1093/mnras/stz3054

Sanderson, R. E., Wetzel, A., Loebman, S., et al. 2020, ApJS, 246, 6, doi: 10.3847/1538-4365/ab5b9d

Schaye, J., Crain, R. A., Bower, R. G., et al. 2015, MNRAS, 446, 521, doi: 10.1093/mnras/stu2058

Sick, J., Courteau, S., Cuillandre, J.-C., et al. 2015, in IAU Symposium, Vol. 311, Galaxy Masses as Constraints of Formation Models, ed. M. Cappellari & S. Courteau, 82–85, doi: 10.1017/S1743921315003440

Simpson, C. M., Grand, R. J. J., Gómez, F. A., et al. 2018, MNRAS, 478, 548, doi: 10.1093/mnras/sty774

Spekkens, K., Urbancic, N., Mason, B. S., Willman, B., & Aguirre, J. E. 2014, ApJL, 795, L5, doi: 10.1088/2041-8205/795/1/L5

Springel, V. 2010, MNRAS, 401, 791, doi: 10.1111/j.1365-2966.2009.15715.x

Springel, V., White, S. D. M., Tormen, G., & Kauffmann, G. 2001, MNRAS, 328, 726, doi: 10.1046/j.1365-8711.2001.04912.x

Springel, V., Pakmor, R., Pillepich, A., et al. 2018, MNRAS, 475, 676, doi: 10.1093/mnras/stx3304

Tamm, A., Tempel, E., Tenjes, P., Tihhonova, O., & Tuvikene, T. 2012, A&A, 546, A4, doi: 10.1051/0004-6361/201220065

Van Der Walt, S., Colbert, S. C., & Varoquaux, G. 2011, Computing in Science & Engineering, 13, 22

Virtanen, P., Gommers, R., Oliphant, T. E., et al. 2020, Nature Methods, 17, 261, doi: 10.1038/s41592-019-0686-2

Watkins, L. L., Evans, N. W., & An, J. H. 2010, MNRAS, 406, 264, doi: 10.1111/j.1365-2966.2010.16708.x

Weinberger, R., Springel, V., Hernquist, L., et al. 2017, MNRAS, 465, 3291, doi: 10.1093/mnras/stw2944

Weisz, D. R., Dalcanton, J. J., Williams, B. F., et al. 2011, ApJ, 739, 5, doi: 10.1088/0004-637X/739/1/5

Wetzel, A. R., Hopkins, P. F., Kim, J.-h., et al. 2016, ApJL, 827, L23, doi: 10.3847/2041-8205/827/2/L23

Wetzel, A. R., Tollerud, E. J., & Weisz, D. R. 2015, ApJL, 808, L27, doi: 10.1088/2041-8205/808/1/L27

Wheeler, C., Phillips, J. I., Cooper, M. C., Boylan-Kolchin, M., & Bullock, J. S. 2014, MNRAS, 442, 1396, doi: 10.1093/mnras/stu965